

1  
2  
3  
4  
5  
6  
7  
8  
9  
10  
11  
12  
13  
14  
15  
16  
17  
18  
19  
20  
21  
22  
23  
24  
25

---

This manuscript has been submitted for publication in **PFG - Journal of Photogrammetry, Remote Sensing and Geoinformation Science**. Please note that, despite having undergone peer-review, the manuscript has yet to be formally accepted for publication. Subsequent versions of this manuscript may have slightly different content. If accepted, the final version of this manuscript will be available via the 'Peer-reviewed Publication DOI' link on the right-hand side of this webpage. Please feel free to contact any of the authors; We welcome feedback.

---

Jayan Wijesingha\*, Thomas Astor, Damian Schulze-Brüninghoff, Michael Wachendorf

**Mapping invasive *Lupinus polyphyllus* Lindl. in semi-natural grasslands using object-based analysis of UAV-borne images**

Grassland Science and Renewable Plant Resources, Universität Kassel,  
Steinstraße 19, D-37213, Witzenhausen, Germany  
jayan.wijesingha@uni-kassel.de (0000-0003-2574-6303), thastor@uni-kassel.de  
(0000-0003-4608-955X), dam.schubrue@uni-kassel.de (0000-0001-8215-975X),  
mwach@uni-kassel.de (0000-0002-2840-7086)

\*Corresponding author: Jayan Wijesingha  
Telephone: +49-561-804-1338  
Mobile phone: +49-177-480-9784  
Email: jayan.wijesingha@uni-kassel.de or gnr@uni-kassel.de

## 26 **Abstract**

27 Knowledge on the spatio-temporal distribution of invasive plant species is vital to maintain  
28 biodiversity in grasslands which are threatened by the invasion of such plants and to evaluate  
29 the effect of control activities conducted. Manual digitising of aerial images with field  
30 verification is the standard method to create maps of the invasive *Lupinus polyphyllus* Lindl.  
31 (Lupine) in semi-natural grasslands of the UNESCO biosphere reserve “Rhön”. As the  
32 standard method is labour- and time-intensive, a workflow was developed to map lupine  
33 coverage using an unmanned aerial vehicle (UAV)-borne remote sensing (RS) along with  
34 object-based image analysis (OBIA). UAV-borne red, green, blue (R, G, B) and thermal  
35 imaging, as well as photogrammetric canopy height modelling (CHM), were applied. Images  
36 were segmented by unsupervised parameter optimisation into image objects representing  
37 lupine plants and grass vegetation. Image objects obtained were classified using random  
38 forest classification modelling based on objects’ attributes. The developed classification model  
39 was employed to create lupine distribution maps of test areas and predicted data were  
40 compared with manually digitised lupine coverage maps. The classification models yielded a  
41 mean prediction accuracy of 89 %, and 0.78 mean kappa statistics. The maximum difference  
42 in lupine area between classified and digitised lupine maps was 5 %. Moreover, the pixel-wise  
43 map comparison showed that 88 % of all pixels matched between classified and digitised  
44 maps. Our results indicate that lupine coverage mapping using UAV-borne RS data and OBIA  
45 provides similar results as the standard manual digitising method and, thus, offers a valuable  
46 tool to map invasive lupine on grasslands.

47 **Keywords:** invasive plant species; *Lupinus polyphyllus* Lindl.; unmanned aerial vehicles;  
48 object-based image analysis; spatial coverage mapping; grassland

## 49 **1. Introduction**

50 Biological invasion is threatening to biodiversity in many ecosystems in the world. The invasion  
51 by alien plant species is considered as one of the significant drivers for loss of biodiversity and  
52 ecosystem functionality. The leading cause for the introduction of alien plant species is human  
53 activities. After a new plant species is introduced to the ecosystem, depending on the  
54 adaptation capability of the plant it obtains a naturalisation status which is the ability to self-  
55 sustain without human involvement (Pyšek and Richardson 2011). At present, there are 3749  
56 naturalised alien plant species in Europe, and 37.4 % out of them occur in grassland habitats  
57 (Lambdon et al. 2008).

58 Processes and dynamics of invasion of plant species are complex (Courchamp et al. 2017).  
59 However, knowledge on the spatial, temporal distribution of invasive plant species in a given  
60 habitat is critical to understand invasion pattern (Müllerová et al. 2017), and maps showing  
61 invasive plants' distribution are helpful for effective control activities. Aerial image digitising  
62 verified with field survey is the standard method to create invasive plant species distribution  
63 maps. Such maps are time-consuming and labour intensive to produce due to aerial image  
64 acquisition, manual digitising, and field verification steps.

65 Classification of remotely sensed images to map invasive species is a well-adopted  
66 technology for many invasive species in different parts of the world and various ecosystems  
67 (Royimani et al. 2018). In grasslands, invasive woody (Mirik et al. 2013) and shrubby (Laliberte  
68 et al. 2004; Ishii and Washitani 2013) species mapping has shown excellent results with  
69 satellite and airborne image classification. Meanwhile, using an unmanned aerial vehicle  
70 (UAV) borne remotely sensed (RS) imaging was increasingly applied for invasive species  
71 mapping in the recent years in flood plains and coastal regions (de Sá et al. 2018; Martin et  
72 al. 2018; Abeysinghe et al. 2019; Jianhui et al. 2019). Cost-effectiveness, high spatial and  
73 temporal resolution and the increasing availability of various miniature sensors (e.g. RGB  
74 cameras, spectral sensors, thermal cameras) are the main advantages of the UAV-borne

75 imaging compared to satellite RS data (Michez et al. 2016). Apart from the spectral or thermal  
76 information, UAV-borne RS data can also provide 3D point cloud data, which can be employed  
77 to derive canopy height models (CHM) for grassland canopies (Grüner et al. 2019; Wijesingha  
78 et al. 2019).

79 UAV-borne RS images are very-high spatial resolution images (less than 50 cm), where one  
80 object in the real world is represented by many pixels. Object-based image analysis (OBIA)  
81 can better be employed when pixels are considerably smaller than the object to be identified  
82 (Blaschke 2010). Several studies indicated that OBIA provides substantial advantages for  
83 mapping invasive plant species based on UAV-borne RS data (Michez et al. 2016; Martin et  
84 al. 2018; Abeysinghe et al. 2019). Typical OBIA employs rules derived from the object's  
85 attributes to classify an object, which requires expert knowledge and limits the transferability  
86 of the classification model (Belgiu et al. 2014). Contrary, machine learning classification  
87 algorithms (e.g. random forest, support vector machine) have shown their capability in OBIA  
88 procedures, as they do not require prior knowledge of the objects (Grippa et al. 2017).

89 *Lupinus polyphyllus* Lindl. (hereafter referred to as lupine) is on the list of the most 150  
90 widespread alien plant species in Europe (Lambdon et al. 2008). The lupine plant is about 50-  
91 150 cm tall and contains 1-2 cm broad leaflets. Lupine flowers are up to 80 cm long in a single  
92 terminal, and they are in shades of blue, pink and white (Fremstad 2010). Lupine is native to  
93 the western parts of North America and has been recorded in many habitats in Europe, such  
94 as grasslands in Germany, Lithuania and at road verges as well as in ruderal areas in  
95 Scandinavia (Fremstad 2010). The UNESCO biosphere reserve Rhön in Germany covers a  
96 total area of 2433 km<sup>2</sup> and mainly consists of low mountain semi-natural grasslands (e.g.  
97 NATURA habitat types 6520 - mountain hay meadows and 6230 - species-rich *Nardus*  
98 grasslands) (Biosphärenreservat Rhön 2019). In the last few decades, lupine invaded  
99 significant parts of the grasslands in the biosphere reserve and substantially changed the  
100 habitat functionality mainly through the ability to fix atmospheric nitrogen, which transforms  
101 the low-growing, open and species-rich grasslands into dense and productive, but species-

102 poor dominance stands (Otte and Maul 2005; Klinger et al. 2019). Individual lupine plants are  
103 controlled manually at early stages of invasion to prevent a massive invasion by lupine, and  
104 grassland mowing is allowed after 1<sup>st</sup> July to maintain a broad diversity of insects and ground  
105 breeding birds (Biosphärenreservat Rhön 2019).

106 The knowledge of the spatial distribution of lupine in the grasslands is vital to conduct control  
107 activities and to monitor their efficacy. The first lupine distribution map of the region was  
108 created in 1998 using manually digitised aerial photographs at a 1:2.500 scale (Otte and Maul  
109 2005). The latest map of the spatial distribution was generated in 2016 using 20 cm digital  
110 ortho-mosaics from aerial photographs (Klinger et al. 2019). Those maps were useful to  
111 monitor changes in the lupine distribution in the long term. The interval between the two maps  
112 of eighteen years is partly due to the time and labour demanding processes involved.  
113 Therefore, a repeatable, transferable methodology is needed, that produces lupine distribution  
114 maps at different spatial and temporal scales to monitor the lupine distribution and to assess  
115 the benefit of control activities.

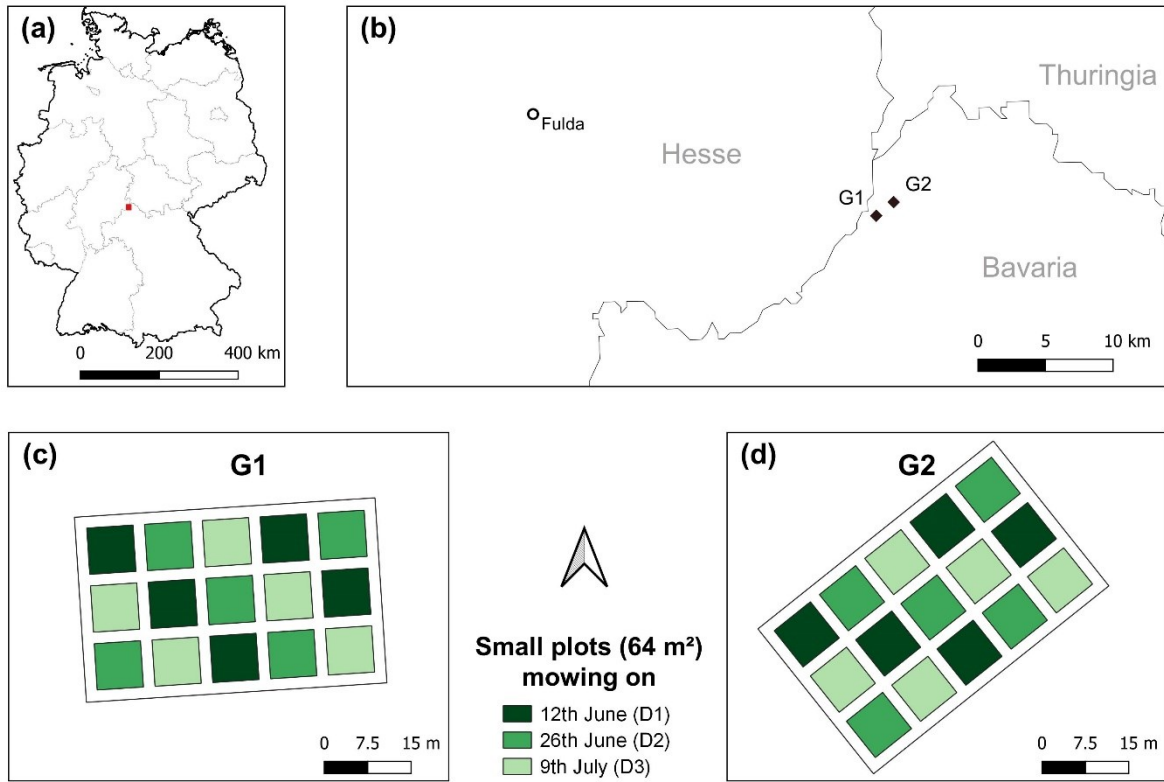
116 According to Skowronek et al., (2018), RS based mapping of the spatial distribution of Lupine  
117 was not successfully implemented until now. In order to fill this gap, we propose an approach  
118 to map invasive lupine in grassland, which is based on UAV-borne RS data and OBIA. We  
119 hypothesise that the proposed procedure could categorise lupine and non-lupine vegetation  
120 in grasslands with the same precision as the standard digitising method. This study presents  
121 an operational workflow to create maps of lupine cover and compares lupine distribution maps  
122 from the developed workflow with manually digitised lupine coverage maps.

## 123 **2. Material and Methods**

### 124 **2.1. Study area**

125 The study was carried out in two grassland fields UNESCO biosphere reserve Röhn in  
126 Germany, which were invaded by lupine (Fig. 1a, Fig. 2). One field was classified as a former  
127 mountain hay meadow (hereafter referred to as G1), and the other was an old *Nardus stricta*  
128 grassland (hereafter referred to as G2). In both fields, rectangle plots of 1500 m<sup>2</sup> (50 m by 30  
129 m) were chosen as study areas, and 15 small plots of 64m<sup>2</sup> (8 m by 8 m) were established  
130 within a grid (Fig. 1c, 1d). Three cutting dates (12<sup>th</sup> June, 26<sup>th</sup> June, 09<sup>th</sup> July, hereafter referred  
131 to as D1, D2, and D3, respectively) were randomly assigned to 5 replicated plots (Fig. 1c, 1d).  
132 At each date, plots were mowed at a stubble height of 5 cm, and biomass was removed from  
133 the field.

134



Administrative boundaries from GDAM data

135

136 **Fig. 1** (a) Location of the UNESCO biosphere reserve Rhön, (b) positions of the two grassland  
 137 fields, and the experimental plot design of (c) G1 and (d) G2 grasslands

138



139

140 **Fig. 2** Lupine invaded grassland in the Röhn biosphere reserve.

141

## 142 **2.2. Data collection**

143 At each sampling date in each grassland field, UAV-borne images were acquired. A DJI-  
144 Phantom IV quadcopter (DJI, China) with an inbuilt off-the-shelf camera (FC330) was  
145 employed to obtain UAV-borne RGB images. The camera (FC330) captures a 12-megapixel  
146 image in red (R), green (G), and blue (B) bands. The UAV was flown at 20 m flying height,  
147 and it resulted in 0.09 m ground sampling distance. The UAV flight mission was designed  
148 using Pix4D capture app for Android (App version 4.4.0, Pix4D, Switzerland). The UAV was  
149 flown as double grid mission (two perpendicular missions), and the camera was triggered  
150 automatically to capture nadir looking images based on the image overlap configuration (80  
151 % both forward and side overlap). All the flight sessions were conducted between 12:00 and  
152 14:00. Before each flight session, nine black and white 1m<sup>2</sup> ground control points were  
153 distributed over the study area. Just after the UAV flights, the position of each ground control  
154 point was measured using a Leica RTK GNSS (Leica Geosystems GmbH, Germany) with 2  
155 cm 3D coordinate precision. Additional UAV-borne RGB image was taken on 16<sup>th</sup> August  
156 2019, when the whole fields were mowed.

157 A FLIR Vue Pro R (FLIR Systems Incorporation, USA) thermal camera was attached to the  
158 UAV parallel to the RGB camera. The camera has a 19 mm lens, and it has a spectral  
159 sensitivity between 7500 - 13500 nm. With a single UAV flight, both thermal and RGB images  
160 were captured simultaneously. The thermal camera captures images as a radiometric JPEG  
161 which contains radiometrically calibrated temperature data. The thermal image has 640 by  
162 512 pixels (FLIR 2016). The thermal camera was triggered every second throughout the whole  
163 UAV mission. Before each thermal data collection, metadata related to the thermal camera  
164 was collected using the FLIR UAS 2 app (App version 2.2.4, FLIR Systems Incorporation,  
165 USA), such as distance to the target (20 m), relative humidity, air temperature, and emissivity  
166 (0.98). All the metadata was saved in each captured image's EXIF data.



167 A total of six UAV-borne RGB and six thermal datasets were collected. Hereafter, each dataset  
168 is labelled according to cutting date and grassland type ( $D_iG_j$ ; where  $i = 1, 2, 3$  and  $j=1, 2$ ). In  
169 each dataset, maturity stages of grasslands were different due to mowing activities in  $64 \text{ m}^2$   
170 small plots. Maturity stage was lowest ( $V_0$ ) in the D1 dataset and was the same for all 30 small  
171 plots. At the 2<sup>nd</sup> cutting date (D2), 20 small plots out of 30 were covered by two weeks older  
172 vegetation ( $V_{2\text{weeks}}$ ), while 10 small plots (which were cut at D1) had vegetation which was  
173 regrown for two weeks ( $VR_{2\text{weeks}}$ ). The D3 dataset was composed of 10 plots with undisturbed  
174 vegetation ( $V_{4\text{weeks}}$ ) which was four weeks older than  $V_0$ , 10 plots of ( $VR_{2\text{weeks}}$ ), and further 10  
175 plots with vegetation regrown for four weeks ( $VR_{4\text{weeks}}$ ) after D1.

176

## 177 **2.3. Object-based image analysis**

### 178 **2.3.1. Canopy height model and point density**

179 Each collected dataset was processed separately, and the same procedure was applied, as  
180 explained below. The UAV-borne RGB images and coordinates of ground control points were  
181 processed with the Agisoft PhotoScan Professional version 1.4.4 software (Agisoft LLC,  
182 Russia). The software applied structure from motion (SFM) technique to align multi-view  
183 overlapping images and to build a dense 3D cloud point. The procedure of point cloud  
184 generation and canopy height computation was adopted from Wijesingha et al. (2019), and  
185 further details of the process can be found there.

186 The point density (PD) raster was created from the dense point cloud by binning into a raster  
187 with 2cm. The PD raster contained point count under a cell area ( $4 \text{ cm}^2$ ). The digital terrain  
188 model (reference plane) was generated using the August RGB images with a cell size raster  
189 of 5 cm. The z values of 3D point cloud and the digital terrain model based on x, y locations  
190 were subtracted to generate a point cloud with canopy height. The point cloud with canopy  
191 height was binned into the 2 cm cell size raster, where each cell contained mean crop height  
192 value and hereafter it was considered CHM raster.

193

### 194 **2.3.2. RGB ortho-mosaic**

195 RGB ortho-mosaic was obtained after further processing of the dense point cloud in  
196 PhotoScan software. The output RGB ortho-mosaic was geo-referenced with a 1 cm spatial  
197 resolution. The RGB ortho-mosaic was converted into hue (H), intensity (I), and saturation (S)  
198 colour model using GRASS GIS and hereafter it was considered as HIS ortho-mosaic  
199 (Gonzalez and Woods 2008; GRASS Development Team 2017).

200

### 201 **2.3.3. Thermal digital ortho-mosaic**

202 The single JPEG thermal image contained 8-bit digital numbers. Following workflow and  
203 equations were adapted from Turner et al. (2017) to convert digital numbers to temperature  
204 values. The conversion workflow was conducted with *EXIFtools* and R programming language  
205 (Phil Harvey 2016; Dunnington and Harvey 2019; R Core Team 2019). A raw thermal TIFF  
206 image was exported from the JPEG image. Metadata of image were extracted from the JPEG  
207 EXIF header for each image. Based on the metadata and raw TIFF image values, the image  
208 with temperature was computed and exported as a TIFF file. The exported TIFF image  
209 contained a calibrated temperature value in degree Celsius (°C). Like RGB ortho-mosaic  
210 generation, thermal ortho-mosaic with 2 cm spatial resolution was generated using calibrated  
211 thermal images.

### 212 **2.3.4. Spectral shape index and texture images**

213 A spectral shape index (SSI) (Equation 1) based on RGB image values were computed, and  
214 it showed excellent results for isolation of shadows within the vegetation (Chen et al. 2009).  
215 Moreover, two texture features (second-order statistics texture namely angular second  
216 moment (ASM) - uniformity, and inverse difference moment (IDM) - homogeneity) (Haralick  
217 1979) from both intensity image and thermal image were computed.

$$SSI = |R + B - 2 \times G| \quad (1)$$

218 where R, G, and B are red, green, and blue values respectively.

### 219 **2.3.5. Segmentation**

220 Segmentation and classification are the two main steps in OBIA (Silver et al. 2019). The  
 221 segmentation is the first step and by definition "it divides an image or any raster or point data  
 222 into spatially continuous, disjoint and homogeneous regions, referred to as segments or image  
 223 objects" (Blaschke et al. 2014). According to Espindola et al., (2006), the quality of  
 224 segmentation depends on the balance between intersegment homogeneity (the similarity  
 225 between segments) and intersegment heterogeneity (the difference between segments).

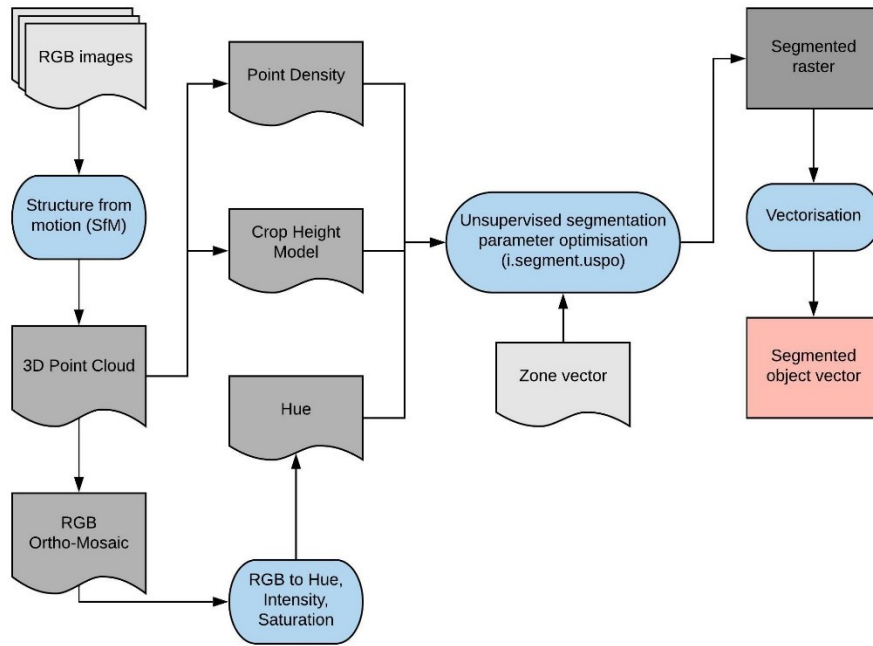
226 Variance and spatial autocorrelation (Moran's I) between segments are utilised as measures  
 227 to evaluate intersegment homogeneity and heterogeneity respectively. A low variance leads  
 228 to over-segmentation of images, as very similar pixels are contained in each segment which  
 229 divides one real-world object into many segments. In contrast, a low spatial autocorrelation  
 230 between segments can increase the variance, and it causes under-segmentation, which gives  
 231 one large segment that covers many different real-world objects. The segmentation threshold  
 232 (also referred to as scale) can control the balance between intersegment variance and spatial  
 233 autocorrelation. Therefore, finding the optimum threshold is essential to produce segments  
 234 which are matching to the real-world objects (Espindola et al. 2006).

235 Johnson et al. (2015) established an F measure to identify the quality of the segmentation  
 236 result for a given threshold value. The F measure is based on variance and spatial  
 237 autocorrelation and calculated using Equation 2 (Johnson et al. 2015). A weight value (alpha)  
 238 must be defined in the F measure, with 0.5 is half weighting, and 2 is double weighting. Like  
 239 the normalise sum measure, the higher the F measure, the higher the quality of the  
 240 segmentation.

$$F = (1 + a^2) \left( \frac{MI_{norm} \times V_{norm}}{a^2 \times MI_{norm} + V_{norm}} \right) \quad (2)$$

241 here  $MI_{norm}$  is the normalised Moran's I value,  $V_{norm}$  is the normalised variance value,  $\alpha$  is the  
242 alpha weight, and F is the F measure.

243 Espindola et al., (2006) introduced the Unsupervised Parameter Optimisation (USPO)  
244 procedure to identify the optimum threshold value for the given image from a range of  
245 threshold values based on one of the quality measures mentioned above. The USPO  
246 procedure was implemented as an add-on tool called *i.segment.uspo* in GRASS GIS software  
247 (Lennert and GRASS Development Team 2019a). The CHM raster, PD raster and hue image  
248 from HIS ortho-mosaic were used in the segmentation process (Fig. 3). According to  
249 Georganos et al. (2018), finding the optimum threshold values for different local image regions  
250 gives superior results compared to the use of a single threshold for the whole image. Hence,  
251 the image was divided into sixteen small zones (15 zones overlapping with the 64 m<sup>2</sup> plots for  
252 each study plot and one zone for the paths between the plots). Specific local thresholds  
253 (ranging from 0.01 to 0.15) was determined for each region based on the F measure. The  
254 alpha value in the F measure calculation was kept at 0.5. Python *Jupyter Notebook* codes  
255 from Grippa (2018) were adopted and modified according to this study for automatizing the  
256 segmentation process using *i.segment.uspo* for each zone. The segmentation procedure was  
257 applied separately for each study plot and sampling date. A total of six different segmented  
258 raster were created according to six datasets.



259

260 **Fig. 3** Flow diagram of the segmentation with *i.segment.uspo* and attribute calculation using  
 261 GRASS GIS

262

### 263 2.3.6. Attribute calculation for segmented image objects

264 The segmented raster was vectorised, and each segmented object was created as a polygon.  
 265 Four geometric attributes (area ( $A$ ), perimeter ( $P$ ), fractional dimension (FD) (Equation 3), and  
 266 circle compactness (CC) (Equation 4)) for the segmented objects were calculated. Based on  
 267 all raster data (RGB image, HIS image, CHM raster, PD raster, thermal image, SSI image,  
 268 and texture raster), the mean and standard deviation values for each polygon was computed  
 269 as image-based attributes. Attribute calculation was done using *i.segment.stats* add-on in  
 270 GRASS GIS (Lennert and GRASS Development Team 2019b). In total, 32 attributes (4  
 271 geometric and 28 image-based) were generated (Table 1).

$$FD = 2 \times \frac{\log P}{\log(A + 0.001)} \quad (3)$$

$$CC = \frac{P}{2 \times \sqrt{\pi \times A}} \quad (4)$$

272

273 Table 1: Description of the calculated object's attributes

ID	Attribute	Description
1	Area	Area of the object
2	Perimeter	Perimeter of the object
3	FD	Fractional dimension of the object
4	CC	Circle compactness of the object
5	Mean R	Mean red image value of the object
6	Mean G	Mean green image value of the object
7	Mean B	Mean blue image value of the object
8	Mean hue	Mean hue image value of the object
9	Mean intensity	Mean intensity image value of the object
10	Mean saturation	Mean saturation image value of the object
11	Mean intensity ASM	Mean intensity ASM texture image value of the object
12	Mean intensity IDM	Mean intensity IDM texture image value of the object
13	Mean SSI	Mean spherical shape index image value of the object
14	Mean temperature	Mean temperature image value of the object
15	Mean thermal ASM	Mean thermal ASM texture image value of the object
16	Mean thermal IDM	Mean thermal IDM texture image value of the object
17	Mean CHM	Mean canopy height model value of the object
18	Mean PD	Mean point density value of the object
19	SD R	Standard deviation of red image value of the object
20	SD G	Standard deviation of green image value of the object
21	SD B	Standard deviation of blue image value of the object
22	SD hue	Standard deviation of hue image value of the object
23	SD intensity	Standard deviation of intensity image value of the object
24	SD saturation	Standard deviation of saturation image value of the object
25	SD intensity ASM	Standard deviation of intensity ASM texture image value of the object
26	SD intensity IDM	Standard deviation of intensity IDM texture image value of the object
27	SD SSI	Standard deviation of spherical shape index image value of the object
28	SD temperature	Standard deviation of temperature image value of the object
29	SD thermal ASM	Standard deviation of thermal ASM texture image value of the object
30	SD thermal IDM	Standard deviation of thermal IDM texture image value of the object
31	SD CHM	Standard deviation of canopy height model value of the object
32	SD PD	Standard deviation of point density value of the object

274

275 **2.3.7. Classification model**

276 Ten percent of the segmented objects (3698 out of a total of 81704 objects) were manually  
 277 labelled as either lupine (L) or non-lupine (NL) based on visual observation using the RGB

278 ortho-mosaics. In each dataset, the number of L and NL labels were very similar (L = 1892  
279 and NL = 1806), and labelled objects were spatially randomised. The labelled objects with  
280 attributes were utilised to develop a supervised classification model.

281 Classification model training and testing were conducted using R statistical software (R Core  
282 Team 2019). The random forest (RF) machine learning classification algorithm was employed  
283 to build a classification model using the *mlr* package in R software (Bischl et al. 2016). The  
284 RF has proven its efficiency for image object classification using objects' attribute data (Belgiu  
285 and Drăgu 2016). The RF algorithm utilises both decision trees and bagging (Breiman 2001).  
286 The decision trees are created from a subset of the training samples with replacement (known  
287 as bagging). Based on the average outcome from the decision trees, the sample is assigned  
288 to a majority class (Belgiu and Drăgu 2016).

289 A total of six RF classification models were built, and in each model, five datasets were  
290 employed to train the model, while the remaining dataset was used to test the model (Table  
291 2). All the attributes (32) were employed as an input of the model along with objects' labels.  
292 Two hyperparameters, namely *mtry* (number of selected variables in each split) and *node size*  
293 (number of observations in a terminal node) (Probst et al. 2019) were tuned in the model  
294 training phase using random search. The model was trained with repeated spatial cross-  
295 validation resampling (five-folds and two repeats) to classify objects. In spatial cross-  
296 validation, the resampling is based on the location of the observations to reduce the effect of  
297 spatial autocorrelation for model accuracy, where it is crucial for spatial-temporal context  
298 (Brenning 2012). The location was based on the centroid of the objects. The trained model  
299 employed to predict objects' labels of the holdout dataset. According to predicted labels and  
300 actual labels, the model performance was evaluated by calculating overall accuracy (OA),  
301 true-positive-rate (TPR), false-positive-rate (FPR), and Kappa (K) values (Equation 5, 6, 7,  
302 and 8 respectively).

303

304 Table 2: Details of the training and testing datasets for different classification models

Model Name	Datasets for training	Dataset for testing
M11	D <sub>1</sub> G <sub>2</sub> , D <sub>2</sub> G <sub>1</sub> , D <sub>2</sub> G <sub>2</sub> , D <sub>3</sub> G <sub>1</sub> , D <sub>3</sub> G <sub>2</sub>	D <sub>1</sub> G <sub>1</sub>
M12	D <sub>1</sub> G <sub>1</sub> , D <sub>2</sub> G <sub>1</sub> , D <sub>2</sub> G <sub>2</sub> , D <sub>3</sub> G <sub>1</sub> , D <sub>3</sub> G <sub>2</sub>	D <sub>1</sub> G <sub>2</sub>
M21	D <sub>1</sub> G <sub>1</sub> , D <sub>1</sub> G <sub>2</sub> , D <sub>2</sub> G <sub>2</sub> , D <sub>3</sub> G <sub>1</sub> , D <sub>3</sub> G <sub>2</sub>	D <sub>2</sub> G <sub>1</sub>
M22	D <sub>1</sub> G <sub>1</sub> , D <sub>1</sub> G <sub>2</sub> , D <sub>2</sub> G <sub>1</sub> , D <sub>3</sub> G <sub>1</sub> , D <sub>3</sub> G <sub>2</sub>	D <sub>2</sub> G <sub>2</sub>
M31	D <sub>1</sub> G <sub>1</sub> , D <sub>1</sub> G <sub>2</sub> , D <sub>2</sub> G <sub>1</sub> , D <sub>2</sub> G <sub>2</sub> , D <sub>3</sub> G <sub>2</sub>	D <sub>3</sub> G <sub>1</sub>
M32	D <sub>1</sub> G <sub>1</sub> , D <sub>1</sub> G <sub>2</sub> , D <sub>2</sub> G <sub>1</sub> , D <sub>2</sub> G <sub>2</sub> , D <sub>3</sub> G <sub>1</sub>	D <sub>3</sub> G <sub>2</sub>

305

$$OA = \frac{TP + TN}{TP + FN + FP + TN} \quad (5)$$

$$TPR = \frac{TP}{TP + FN} \quad (6)$$

$$FPR = \frac{FP}{FP + TN} \quad (7)$$

$$K = \frac{\text{Observed agreement} - \text{Expected agreement}}{1 - \text{Expected agreement}} \quad (8)$$

306 Where TP is true positives, TN is true negative, FP is false-positive, and FN is false-negative.

307

## 308 2.4. Lupine coverage mapping

309 A single RF classification model ( $M_{all}$ ) was trained using all labelled objects from the six  
 310 datasets. Based on predicted labels from  $M_{all}$ , a lupine coverage map was generated  
 311 (hereafter referred to as classification-based lupine coverage map).

312 A reference lupine coverage map for each dataset was created by digitising each RGB ortho-  
 313 mosaic and was compared to the lupine area from the classification-based lupine coverage  
 314 map. A relative number of no-difference pixels from two maps was computed as a measure  
 315 for map accuracy (MA) (Equation 9). Additionally, the pixel-wise correlation coefficient (PCC)  
 316 was calculated. Each 64 m<sup>2</sup> plot was divided into four equal areas of 16m<sup>2</sup> each, and the



317 relationship between relative digitised lupine area (LA) and MA of subdivided plots was  
318 analysed to understand the MA at different levels of LA.

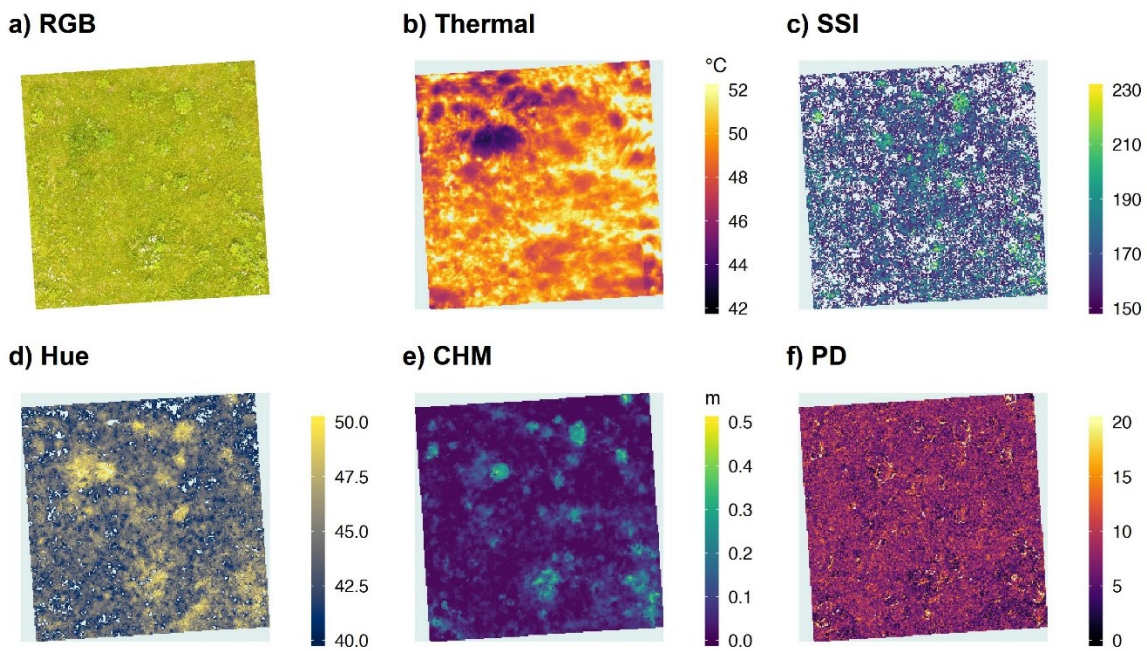
$$MA = \frac{\textit{Number of equally categorised pixels in the two maps}}{\textit{Total number of pixels}} \times 100 \quad (9)$$

319

320 **3. Results**

321 **3.1. Image segmentation**

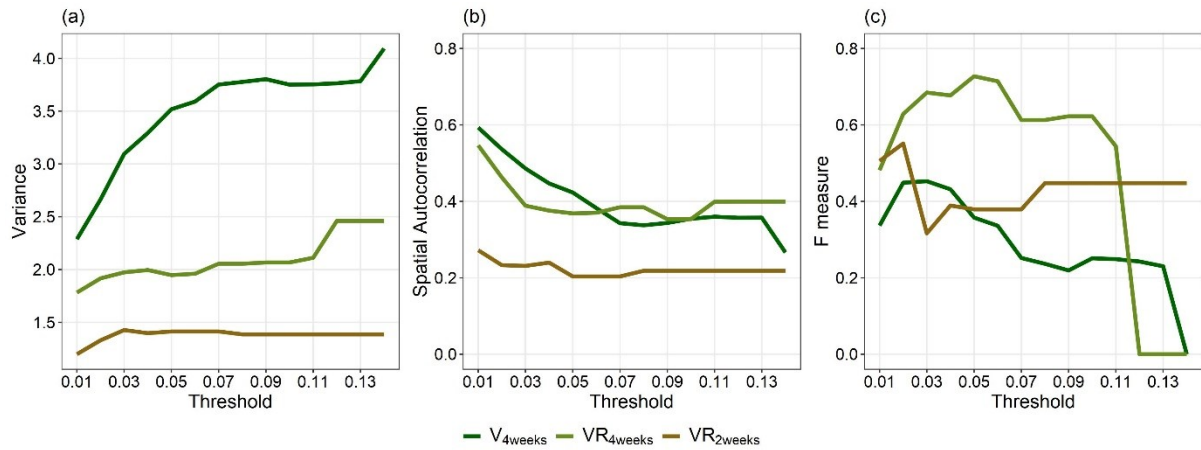
322 Ortho-mosaics from RGB and thermal camera images were created in this study and SSI, and  
323 hue images were computed from the RGB ortho-mosaic. RGB images were processed with  
324 SFM technique to generate CHM raster and PD raster. Exemplary images and raster from D1  
325 of G1 are shown in Fig. 4.



326

327 **Fig. 4** Exemplary images for D1G1 (Field G1, 12<sup>th</sup> June) dataset (a) RGB digital ortho-mosaic,  
328 (b) Thermal digital ortho-mosaic, (c) spectral shape index (SSI) image, (d) hue image, (e)  
329 canopy height model (CHM) raster, and (f) point density (PD) raster

330 The CHM raster, PD raster, and hue image were utilised to create image objects. The optimum  
331 threshold values for different image regions were determined using USPO. As shown in Fig.  
332 5, three image regions with different vegetation maturity obtained distinct optimum threshold  
333 values. Example segmented image is shown in the Appendix (Fig. 9).



334

335 **Fig. 5** Course of (a) variance, (b) spatial autocorrelation, and (c) F measure values for different  
 336 threshold values in three different image regions where VR<sub>4weeks</sub>: regrown vegetation 4 weeks  
 337 after mowing, VR<sub>2weeks</sub>: regrown vegetation 2 weeks after mowing, and V<sub>4weeks</sub>: vegetation four  
 338 weeks older than 12<sup>th</sup> June vegetation

339

### 340 3.2. Classification model training and testing

341 Six classification models were trained while holding out one dataset at each time. The model  
 342 results are summarised in Table 3. Based on the all performance measures in model testing  
 343 phase, model M12 (model tested with D<sub>1</sub>G<sub>2</sub> data) obtained the lowest performances (OA =  
 344 78.2 %, K = 0.55) and model M32 (model tested with D<sub>3</sub>G<sub>2</sub> data) achieved the highest values  
 345 (OA = 97.2 %, K = 0.94). Although model M12 accurately classified all lupine objects (100 %  
 346 TPR), it also categorised nearly half of the non-lupine objects as lupine objects (47.3 % FPR).  
 347 Additionally, models that tested with D1 data (M11 and M12) obtained slightly lower  
 348 performances compared to other models.

349 Table 3: Classification model results (L: lupine, NL: non-lupine, TA: training accuracy, OA:  
 350 overall accuracy, K: Kappa statistics, TPR: true-positive rate, FNR: false-negative rate)

Model	Training	Testing				
	No. of objects	No. of objects	OA (%)	TPR (%)	FPR (%)	K
M11	L = 1581; NL = 1545	L = 311; NL = 261	83.2	76.8	9.2	0.67
M12	L = 1394; NL = 1381	L = 498; NL = 425	78.2	100.0	47.3	0.55
M21	L = 1578; NL = 1429	L = 314; NL = 377	90.6	84.1	4.0	0.81
M22	L = 1701; NL = 1638	L = 191; NL = 168	96.4	95.8	3.0	0.93

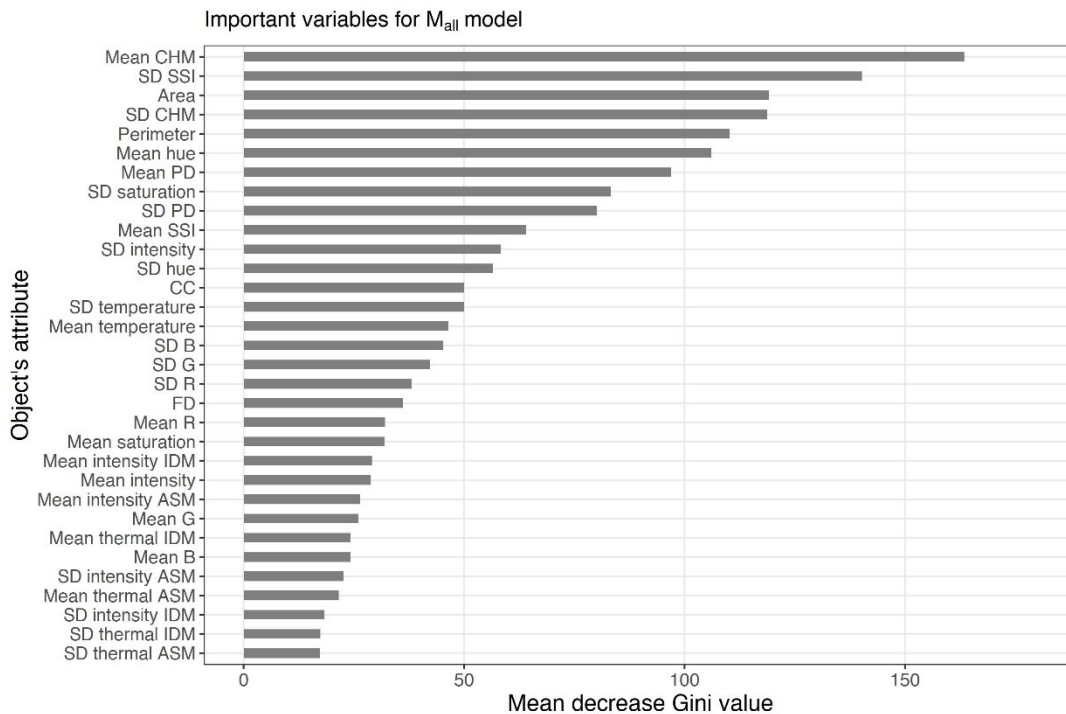
M31	L = 1530; NL = 1405	L = 362; NL = 401	90.1	88.4	6.7	0.82
M32	L = 1676; NL = 1632	L = 216; NL = 174	97.2	96.7	2.3	0.94

351

### 352 3.3. Final classification model and important attributes

353 After testing six classification models with the different spatial-temporal dataset, the complete  
 354 classification model ( $M_{all}$ ) was trained using all available data (3698 objects) with spatial cross-  
 355 validation. The  $M_{all}$  model achieved 94.2 % training accuracy.

356 The importance of the objects' attributes to the  $M_{all}$  classification model was assessed based  
 357 on the mean decrease Gini value (Fig. 6). It is based on "the total decrease in node impurities  
 358 from splitting on the variable, averaged over all trees" (Liaw and Wiener 2002). The six most  
 359 important variable of the model were *Mean CHM*, *SD SSI*, *Area*, *SD CHM*, *Perimeter*, and  
 360 *mean hue* attribute values. Attributes related to texture features were the least essential  
 361 prediction variables to the  $M_{all}$  model.



362

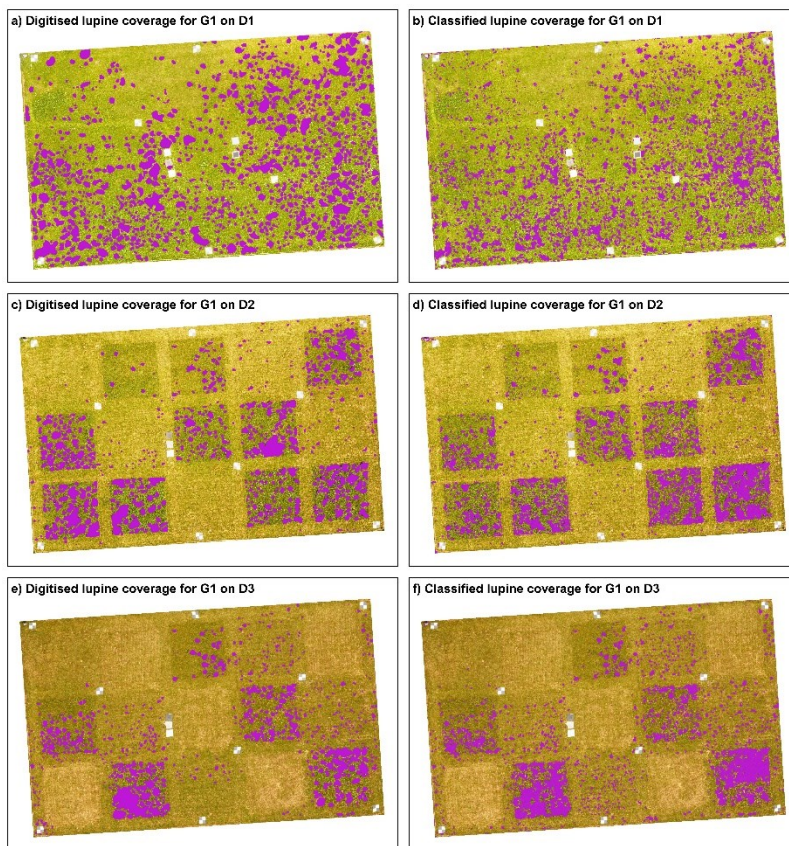
363 **Fig. 6** Important object's attributes for the  $M_{all}$  classification model (complete model) based on  
 364 mean decrease Gini values

365

### 366 3.4. Lupine coverage maps

367 Based on visual observation between digitised lupine map and classified lupine map, both  
368 maps showed similar visual representation. Fig. 7 illustrates lupine coverage maps from both  
369 digitising and classification for three sampling dates (D1, D2, D3) in G1 field. However, the  
370 area-based comparison showed maximum  $\pm 5\%$  of the change in total lupine coverage (Table  
371 4).

372



373

374 **Fig. 7** Lupine coverage map of the G1 field with a, c, e, showing manually digitised lupine  
375 cover (purple) at D1 (12<sup>th</sup> June), D2 (26<sup>th</sup> June), and D3 (9<sup>th</sup> July) and b, d, f, showing lupine  
376 cover classified by UAV-borne RS data and OBIA

377

378

379 The classification based lupine coverage was assessed against reference lupine coverage  
 380 map using comparing pixels in two raster maps. From comparison results, map accuracy  
 381 relative to the reference map and CC was computed (Table 4). According to raster comparison  
 382 results, D1 dataset obtained the lowest MA (80.4 %, 80.9 %) and PCC (0.40, 0.50) values in  
 383 G1 and G2 fields respectively. The MA and CC values tended to increase with reducing lupine  
 384 coverage. However, comparison results for G2 dataset always indicated slightly better results  
 385 than G1.

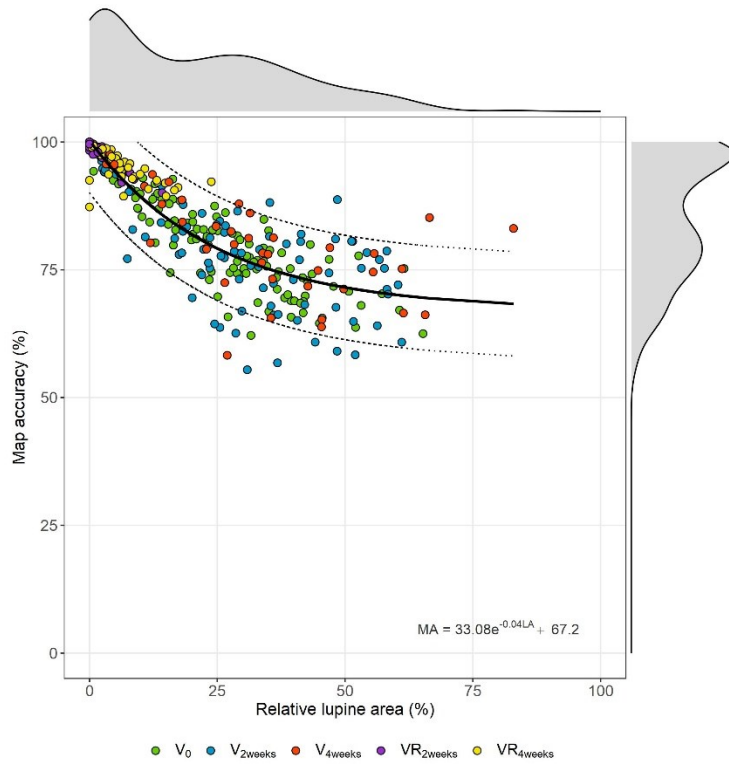
386

387 Table 4: Pixel-based comparison between manually digitised and classified lupine coverage.  
 388 (LA: lupine area, MA: map accuracy, PCC: pixel-wise correlation coefficient)

Date	Field	LA	Relative LA difference	MA	PCC
D1	G1	294 m <sup>2</sup>	-5 %	80.4 %	0.40
	G2	443 m <sup>2</sup>	+3 %	80.9 %	0.50
D2	G1	237 m <sup>2</sup>	+1 %	88.7 %	0.52
	G2	308 m <sup>2</sup>	+3 %	89.0 %	0.61
D3	G1	188 m <sup>2</sup>	+2 %	93.1 %	0.63
	G2	181 m <sup>2</sup>	+2 %	93.8 %	0.68

389

390 Relationship between the relative LA and MA indicated a negative exponential trend (Fig. 8).  
 391 The correlation coefficient between relative LA and MA was -0.88, and trend line had 0.80  
 392 goodness of fit. Regardless of the vegetation maturity, the explained relationship was valid.  
 393 Until LA reached 25 %, it showed a strong relationship with MA, but over 25 % LA the MA  
 394 values were scattered around the regression curve.



395

396 **Fig. 8** The relationship between relative lupine area (LA) from manual digitising and map  
 397 accuracy (MA) based on the generalised model, comprising undisturbed/not mowed  
 398 vegetation ( $V_0$ ,  $V_{2weeks}$ ,  $V_{4weeks}$ ), and regrown vegetation after mowing ( $VR_{2weeks}$ ,  $VR_{4weeks}$ )

399

## 400 **4. Discussion**

401 Invasion by lupine endangers biodiversity and ecosystem functionality (Otte and Maul 2005;  
402 Klinger et al. 2019). The spatial and temporal distribution of lupine is essential to understand  
403 the invasive pattern, to plan appropriate management strategies and to monitor the impact of  
404 control actions. While RS was utilised to map several invasive plant species (e.g. *Impatiens*  
405 *glandulifera*, *Spartina anglica*, *Solidago canadensis*), invasion patterns of lupine were not  
406 examined until now (Skowronek et al. 2018). This study aimed to develop an operational  
407 workflow to map the spatial distribution of invasive lupine in grasslands using UAV-borne  
408 imageries and OBIA.

409 OBIA has shown its' effectiveness to work with very high-resolution (< 1 m spatial resolution)  
410 images, where several pixels represent one object rather than classifying each pixel  
411 separately. While OBIA allowed taking advantage of RGB images only, a pixel-based  
412 classification approach would have demanded spectral signatures. Segmentation is the critical  
413 step in the OBIA. The first step of the proposed workflow was to segment collected UAV-borne  
414 images into image objects that represent either lupine or non-lupine (i.e. mainly grass) plants.  
415 USPO based area-specific threshold values benefitted for obtaining good object delineation  
416 (Fig. 5). However, USPO for a multitude of image areas leads to an increased computational  
417 time corresponding to the size of the areas and the spatial resolution of the images  
418 (Georganos et al. 2018).

419 Apart from optimal threshold identification, different combinations of various raster types were  
420 tested (data not shown). Visual assessment of the segments obtained suggested that the  
421 combined raster with CHM, PD and hue data provided the best segmentation results. This is  
422 comprehensible, as the canopy height of lupine plants is usually taller than the surrounding  
423 grass vegetation (Otte and Maul 2005), also resulting in higher point densities at the edges of  
424 the lupine plant than in the plants' centres. Therefore, CHM and PD raster data significantly  
425 contributed to the delineation of objects and the contour like pattern can be seen from



426 segmented raster (Appendix Fig. 9). CHM data has been utilised recently as classification  
427 variable for invasive species mapping (Jones et al. 2011; Lehmann et al. 2017), but this is the  
428 first study where CHM data was employed to delineate objects in invasive species mapping.  
429 Additionally, hue data derived from RGB images characterised the degree of pureness of the  
430 colour compared to the primary colours (Gonzalez and Woods, 2008) also assisted in defining  
431 object boundaries.

432 Random forest classification models with 32 attributes as predictors were trained and tested  
433 based on different datasets. The model M12 obtained the highest TPR but got the lowest FPR  
434 and tended to over-classify non-lupine objects as lupine objects. As the M12 model was tested  
435 with datasets containing only young lupine plants, small objects that were not lupine may have  
436 been overestimated. This may also be true for the M11 model, which had a similarly low  
437 accuracy compared to the other models. Overall, the performance of the six models showed  
438 high model stability and robustness across time and space, which indicates that the models  
439 could be transferred easily to other grassland sites of varying maturity. As demonstrated with  
440 previous studies (Belgiu and Drăgu 2016), our results confirmed that RF modelling creates  
441 robust algorithms to use object classification in OBIA for vegetation mapping.

442 Several attributes related to plant structure or architecture as well as colour were essential  
443 predictors in the  $M_{all}$  model. The height difference between lupine plants and grass vegetation  
444 contributed to the classification of segmented objects. It points at a prominent advantage of  
445 UAV-borne RS, which allows the separation of two plant types by CHM attributes. This was  
446 also proven by other studies that utilised CHM from UAV-borne RS data to map invasive  
447 species mapping (i.e. *Phragmites australis* in estuaries by Abeysinghe et al. (2019) and  
448 *Fallopia* spp. in floodplains by Martin et al. (2018)).

449 Segment's area and perimeter were further vital geometric features in the final classification  
450 model, whereas fractional dimensions and circle compactness were not useful. A closer look  
451 at the segmented objects shows that area (average values were 0.04 m<sup>2</sup> and 0.17 m<sup>2</sup> for L  
452 and NL objects respectively) and perimeter (average values were 1.6 m and 3.5 m for L and

453 NL objects respectively) of lupine objects were substantially smaller compared to non-lupine  
454 objects, irrespective of the lupine coverage (Appendix Fig. 10). The automated process  
455 segmented lupine objects always in relatively small areas even when large parts of the area  
456 were covered by lupine. Our findings confirm results from other studies, where area and  
457 perimeter were essential variables in discrimination models, e.g. species mapping in arid  
458 areas as demonstrated by Silver et al. (2019).

459 To reduce the computation complexity, only two texture parameters (angular second moment,  
460 inverse difference moment) were computed out of many existing parameters. Surprisingly, all  
461 four texture attributes (intensity-based and thermal-based) were ineffective in our study.  
462 Previous studies (Chabot et al., 2018; Silver et al., 2019) with OBIA have proven that textural  
463 information was useful. However, they utilised many more texture attributes than employed in  
464 our study. Hence, the accuracy of our models might be increased by including further texture  
465 parameters.

466 Corresponding to the intense green colour of lupine leaves and pronounced red and blue  
467 shades of flowers, SSI values computed from RGB intensities indicated higher values in leafy  
468 areas and lower values in regions, where flowering lupines dominated. Consequently, an  
469 increased cover of lupine plants at different maturity stages resulted in increased standard  
470 deviations of SSI, due to a broader distribution of the SSI values (Appendix Fig. 10). This may  
471 explain why the variation of standard deviation values among objects supported the  
472 categorisation of lupine and non-lupine objects.

473 As lupine plants contain higher water contents compared to grasses (Hensgen and  
474 Wachendorf 2016), lupine containing areas in thermal images showed lower temperatures  
475 compared to the surrounding grass area (Fig. 4b). Additionally, the bushy structure of lupine  
476 plants creates shaded areas in the surrounding, which may have further decreased  
477 temperature. Surprisingly, temperature-related attributes (temperature or texture attributes  
478 from thermal image) did not become significant predictors in the classification models.  
479 Evidently, other predictors were of superior relevance than the temperature attributes.

480 However, this leads to reduced costs for sensors and platforms as well as model complexity  
481 and computing time.

482 As relative LA increased, the MA of the lupine coverage maps that generated from our  
483 workflow decreased (Fig. 8). The negative relationship was valid for both undisturbed  
484 vegetation of different maturity and regrown vegetation after mowing. With an increasing  
485 lupine area, the classification procedure tends to over-estimate lupine coverage due to  
486 difficulty to separate lupine and grass vegetation. In general, early detection of invasive plant  
487 species and rapid action is critical to control invasive species (Cock and Wittenberg 2001).  
488 Similarly, for lupine management activities, ecologists prefer to act in regions with lower lupine  
489 coverage, as at this stage of invasion, eradication and containment are easier than high lupine  
490 coverage regions. Since maps with lower lupine coverage were accurate, ecologists can  
491 identify regions with relatively small lupine coverage and precisely locate single lupine plants  
492 for eradication.

493 Though it could be shown that the proposed method performed as well as the standard  
494 digitising method, it may be criticised that vegetation mapping based on UAV-borne RS data  
495 is challenging to scale up (e.g. Chabot et al., 2018). In this study, one UAV flight took 20  
496 minutes (including ground preparation and flight time) to collect data of approximately 0.4  
497 hectares (without thermal sensor). The conduction of additional flight sessions, as well as  
498 expected advance in sensor and platform technology, may lead to an increased data  
499 acquisition area in the future. The proposed method can be considered cost-efficient, as it only  
500 requires a standard UAV-mounted RGB camera, and as most of the utilised software is free  
501 and open-source (GRASS GIS, R, QGIS), except the Agisoft PhotoScan software, which could  
502 be replaced with available free software (e.g. open drone map).

503 Our proposed classification approach can easily be applied in other comparable  
504 environments, as the model was trained with heterogeneous datasets from commonly  
505 occurring grassland vegetation at different stages of maturity. The spatial lupine coverage  
506 maps that were created can be utilised i) to identify the distribution of lupine in grasslands, ii)

507 to estimate the size and degree of lupine invasion by comparing maps generated in different  
508 years, and iii) to evaluate the effectiveness of lupine control. As suggested by Kattenborn et  
509 al., (2019), UAV-borne lupine coverage maps can further be employed for the creation of field  
510 samples to train and test satellite image-based models for invasive lupine mapping in larger  
511 areas.

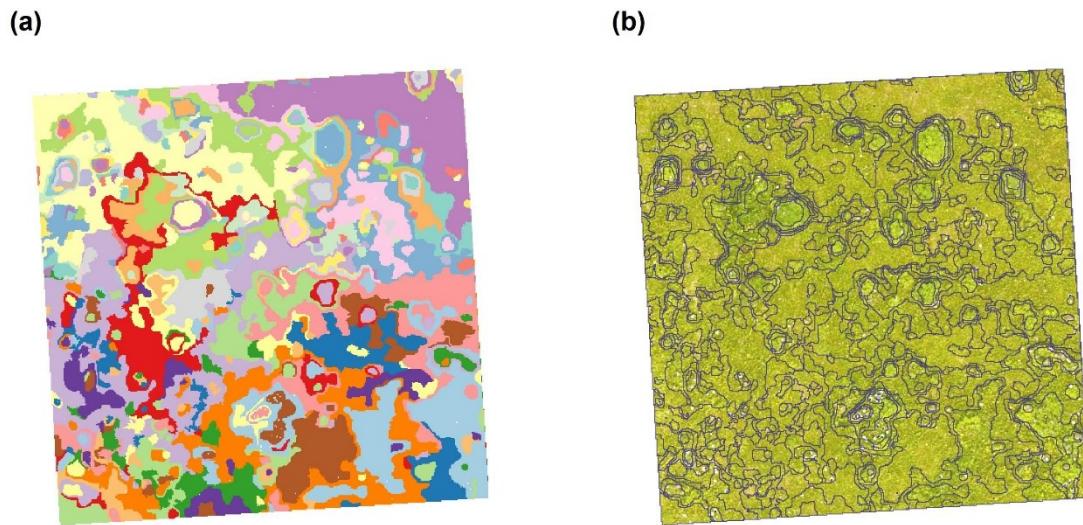
## 512 **5. Conclusion**

513 Gaining knowledge on the spatio-temporal distribution of lupine is vital to maintain biodiversity  
514 in grasslands which are threatened by the invasion of this plant. We successfully developed a  
515 workflow that can accurately map lupine coverage in a grassland using UAV-borne RS and  
516 OBIA. In our proposed workflow, we developed a robust RF classification model that can  
517 classify lupine and non-lupine image objects. The resulting maps showed a  $\pm 5$  % discrepancy  
518 in the lupine area compared to the standard digitising method. Moreover, the classification  
519 model can be transferred to other regions, and thereby overcomes limitations of the standard  
520 way of lupine mapping. Finally, the developed procedure can be adopted for mapping other  
521 invasive species.

522

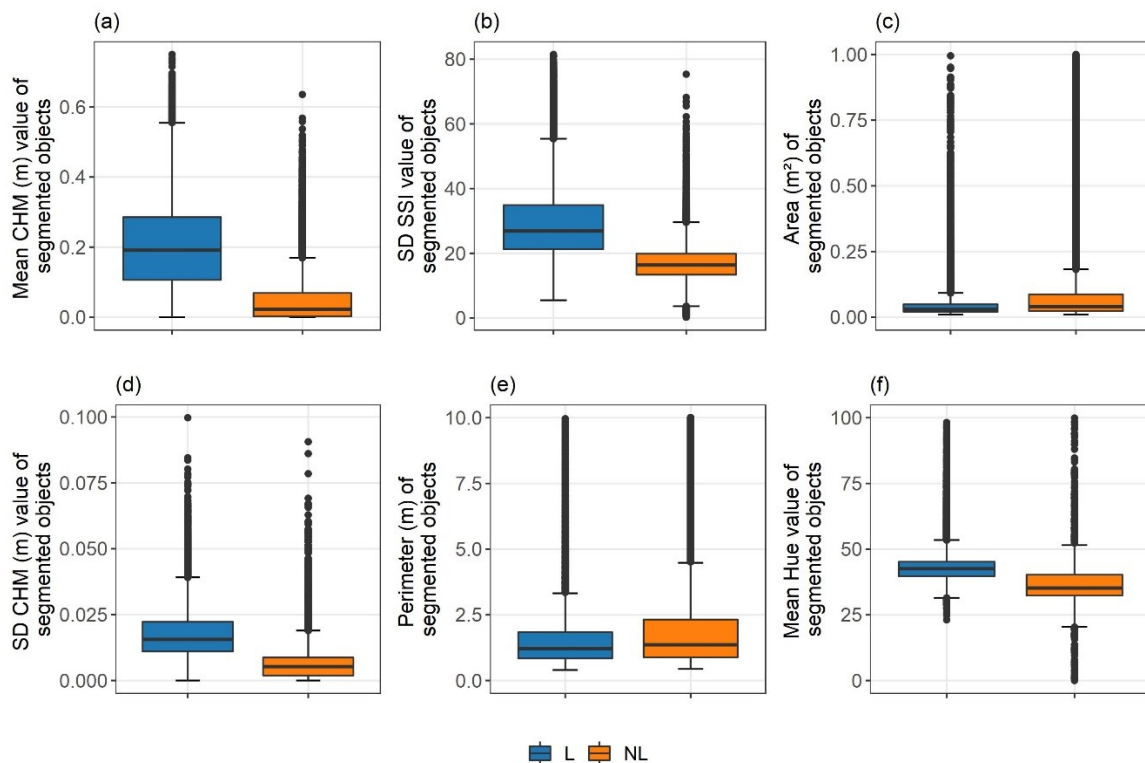
## 523 **Acknowledgement**

524 This research was supported by the German Federal Environmental Foundation (Deutsche  
525 Bundesstiftung Umwelt - DBU). The authors would like to thank Frank Hensgen, Felix Voll,  
526 and Oliver Becker for their help in the field data collection, and to Estefania Duque Perez for  
527 helping with image digitising. We are also grateful to the government of Bavaria for permission  
528 to conduct our measurements in a nature conservation area.



530

531 **Fig. 9** Subset of the (a) segmented object raster (unique colour represents a single segmented  
 532 object and colours are repeated), and (b) vectorised segmented object overlay with RGB  
 533 image for G<sub>1</sub>D<sub>1</sub> (Field G1, 12<sup>th</sup> June) dataset



534

535 **Fig. 10** Distribution of the values of the most six significant predictors in the classification  
 536 model for Lupine (L), and non-Lupine (NL) category. (a) mean canopy height model values,  
 537 (b) standard deviation values of spectral shape index, (c) area values, (d) standard deviation  
 538 values of canopy height model, (e) perimeter values, and (f) mean hue values

539

540 **Reference**

- 541 Abeysinghe T, Milas AS, Arend K, et al (2019) Mapping invasive *Phragmites australis* in the  
542 Old Woman Creek estuary using UAV remote sensing and machine learning classifiers.  
543 *Remote Sens* 11:23. <https://doi.org/10.3390/rs11111380>
- 544 Belgiu M, Drăgu L (2016) Random forest in remote sensing: A review of applications and  
545 future directions. *ISPRS J Photogramm Remote Sens* 114:24–31.  
546 <https://doi.org/10.1016/j.isprsjprs.2016.01.011>
- 547 Belgiu M, Drăguț L, Strobl J (2014) Quantitative evaluation of variations in rule-based  
548 classifications of land cover in urban neighbourhoods using WorldView-2 imagery.  
549 *ISPRS J Photogramm Remote Sens* 87:205–215.  
550 <https://doi.org/10.1016/j.isprsjprs.2013.11.007>
- 551 Biosphärenreservat Rhön (2019) Biosphärenreservat Rhön. [https://biosphaerenreservat-](https://biosphaerenreservat-rhoen.de/)  
552 [rhoen.de/](https://biosphaerenreservat-rhoen.de/). Accessed 8 Oct 2019
- 553 Bischl B, Lang M, Kotthoff L, et al (2016) Mlr: Machine learning in R. *J Mach Learn Res*  
554 17:1–5
- 555 Blaschke T (2010) Object based image analysis for remote sensing. *ISPRS J Photogramm*  
556 *Remote Sens* 65:2–16. <https://doi.org/10.1016/j.isprsjprs.2009.06.004>
- 557 Blaschke T, Hay GJ, Kelly M, et al (2014) Geographic Object-Based Image Analysis -  
558 Towards a new paradigm. *ISPRS J Photogramm Remote Sens* 87:180–191.  
559 <https://doi.org/10.1016/j.isprsjprs.2013.09.014>
- 560 Breiman L (2001) Random forests. *Mach Learn* 45:5--32
- 561 Brenning A (2012) Spatial cross-validation and bootstrap for the assessment of prediction  
562 rules in remote sensing: The R package sperrorest. *Int Geosci Remote Sens Symp*  
563 5372–5375. <https://doi.org/10.1109/IGARSS.2012.6352393>

564 Chabot D, Dillon C, Shemrock A, et al (2018) An object-based image analysis workflow for  
565 monitoring shallow-water aquatic vegetation in multispectral drone imagery. *ISPRS Int J*  
566 *Geo-Information* 7:. <https://doi.org/10.3390/ijgi7080294>

567 Chen Y, Su W, Li J, Sun Z (2009) Hierarchical object oriented classification using very high  
568 resolution imagery and LIDAR data over urban areas. *Adv Sp Res* 43:1101–1110.  
569 <https://doi.org/10.1016/j.asr.2008.11.008>

570 Cock MJW, Wittenberg R (2001) Early detection. In: Cock MJW, Wittenberg R (eds) *Invasive*  
571 *alien species: a toolkit of best prevention and management practices*. CAB  
572 International, Wallingford, pp 101–123

573 Courchamp F, Fournier A, Bellard C, et al (2017) Invasion biology: Specific problems and  
574 possible solutions. *Trends Ecol Evol* 32:13–22.  
575 <https://doi.org/10.1016/j.tree.2016.11.001>

576 de Sá NC, Castro P, Carvalho S, et al (2018) Mapping the flowering of an invasive plant  
577 using unmanned aerial vehicles: Is there potential for biocontrol monitoring? *Front Plant*  
578 *Sci* 9:1–13. <https://doi.org/10.3389/fpls.2018.00293>

579 Dunnington D, Harvey P (2019) *exifr: EXIF Image Data in R*

580 Espindola GM, Camara G, Reis IA, et al (2006) Parameter selection for region-growing  
581 image segmentation algorithms using spatial autocorrelation. *Int J Remote Sens*  
582 27:3035–3040. <https://doi.org/10.1080/01431160600617194>

583 FLIR (2016) *FLIR Vue Pro and Vue Pro R User Guide*

584 Fremstad E (2010) NOBANIS - Invasive alien species fact sheet. In: Online Database Eur.  
585 Netw. Invasive Alien Species – NOBANIS. <http://www.nobanis.org/>. Accessed 7 Oct  
586 2019

587 Georganos S, Grippa T, Lennert M, et al (2018) Scale matters: Spatially partitioned  
588 unsupervised segmentation parameter optimization for large and heterogeneous



589 satellite images. *Remote Sens* 10:. <https://doi.org/10.3390/rs10091440>

590 Gonzalez RC, Woods RE (2008) Color image processing. In: Gonzalez RC, Woods RE (eds)  
591 Digital image processing, Third Edit. Pearson Education, New Jersey, pp 401–414

592 GRASS Development Team (2017) Geographic Resources Analysis Support System  
593 (GRASS GIS) Software, Version 7.2

594 Grippa T (2018) Opensource OBIA processing chain

595 Grippa T, Lennert M, Beaumont B, et al (2017) An open-source semi-automated processing  
596 chain for urban object-based classification. *Remote Sens* 9:.  
597 <https://doi.org/10.3390/rs9040358>

598 Grüner E, Astor T, Wachendorf M (2019) Biomass prediction of heterogeneous temperate  
599 grasslands using an SfM approach based on UAV imaging. *Agronomy* 9:54.  
600 <https://doi.org/10.3390/agronomy9020054>

601 Haralick RM (1979) Statistical and structural approaches to texture. *Proc IEEE* 67:786–804.  
602 <https://doi.org/10.1109/PROC.1979.11328>

603 Hensgen F, Wachendorf M (2016) The effect of the invasive plant species *lupinus*  
604 *polyphyllus* Lindl. On energy recovery parameters of semi-natural grassland biomass.  
605 *Sustain* 8:. <https://doi.org/10.3390/su8100998>

606 Ishii J, Washitani I (2013) Early detection of the invasive alien plant *Solidago altissima* in  
607 moist tall grassland using hyperspectral imagery. *Int J Remote Sens* 34:5926–5936.  
608 <https://doi.org/10.1080/01431161.2013.799790>

609 Jianhui L, Dingquan L, Gui Z, et al (2019) Study on extraction of foreign invasive species  
610 *Mikania micrantha* based on unmanned aerial vehicle (UAV) hyperspectral remote  
611 sensing. In: Fifth Symposium on Novel Optoelectronic Detection Technology and  
612 Application. p 53

613 Johnson BA, Bragais M, Endo I, et al (2015) Image segmentation parameter optimization  
614 considering within-and between-segment heterogeneity at multiple scale levels: Test  
615 case for mapping residential areas using landsat imagery. ISPRS Int J Geo-Information  
616 4:2292–2305. <https://doi.org/10.3390/ijgi4042292>

617 Jones D, Pike S, Thomas M, Murphy D (2011) Object-based image analysis for detection of  
618 Japanese Knotweed s.l. taxa (polygonaceae) in Wales (UK). Remote Sens 3:319–342.  
619 <https://doi.org/10.3390/rs3020319>

620 Kattenborn T, Lopatin J, Förster M, et al (2019) UAV data as alternative to field sampling to  
621 map woody invasive species based on combined Sentinel-1 and Sentinel-2 data.  
622 Remote Sens Environ 227:61–73.  
623 <https://doi.org/https://doi.org/10.1016/j.rse.2019.03.025>

624 Klinger YP, Harvolk-scho S, Otte A, Ludewig K (2019) Applying landscape structure analysis  
625 to assess the spatio-temporal distribution of an invasive legume in the Rho UNESCO  
626 Biosphere Reserve. 21:2735–2749. <https://doi.org/10.1007/s10530-019-02012-x>

627 Laliberte AS, Rango A, Havstad KM, et al (2004) Object-oriented image analysis for  
628 mapping shrub encroachment from 1937 to 2003 in southern New Mexico. Remote  
629 Sens Environ 93:198–210. <https://doi.org/10.1016/j.rse.2004.07.011>

630 Lambdon PW, Pyšek P, Basnou C, et al (2008) Alien flora of Europe: Species diversity,  
631 temporal trends, geographical patterns and research needs. Preslia 80:101–149

632 Lehmann JRKK, Prinz T, Ziller SR, et al (2017) Open-source processing and analysis of  
633 aerial imagery acquired with a low-cost Unmanned Aerial System to support invasive  
634 plant management. Front Environ Sci 5:1–16. <https://doi.org/10.3389/fenvs.2017.00044>

635 Lennert M, GRASS Development Team (2019a) Addon i.segment.uspo. Geographic  
636 resources analysis support system (GRASS) software, version 7.6.  
637 <https://grass.osgeo.org/grass76/manuals/addons/i.segment.uspo.html>. Accessed 16

638 Oct 2019

639 Lennert M, GRASS Development Team (2019b) Addon i.segment.stats. Geographic  
640 resources analysis support system (GRASS) software, version 7.6.  
641 <https://grass.osgeo.org/grass76/manuals/addons/i.segment.stats.html>. Accessed 18  
642 Oct 2019

643 Liaw A, Wiener M (2002) Classification and Regression by randomForest. R J 2:18–22.  
644 <https://doi.org/10.1177/154405910408300516>

645 Martin FM, Müllerová J, Borgniet L, et al (2018) Using single- and multi-date UAV and  
646 satellite imagery to accurately monitor invasive knotweed species. Remote Sens 10:.  
647 <https://doi.org/10.3390/rs10101662>

648 Michez A, Piégay H, Jonathan L, et al (2016) Mapping of riparian invasive species with  
649 supervised classification of Unmanned Aerial System ( UAS ) imagery. Int J Appl Earth  
650 Obs Geoinf 44:88–94. <https://doi.org/10.1016/j.jag.2015.06.014>

651 Mirik M, Chaudhuri S, Surber B, et al (2013) Detection of two intermixed invasive woody  
652 species using color infrared aerial imagery and the support vector machine classifier. J  
653 Appl Remote Sens 7:073588. <https://doi.org/10.1117/1.jrs.7.073588>

654 Müllerová J, Brůna J, Bartaloš T, et al (2017) Timing is important: Unmanned aircraft vs.  
655 Satellite imagery in plant invasion monitoring. Front Plant Sci 8:1–13.  
656 <https://doi.org/10.3389/fpls.2017.00887>

657 Otte A, Maul P (2005) Verbreitungsschwerpunkte und strukturelle Einnischung der Stauden-  
658 Lupine (*Lupinus polyphyllus* Lindl.) in Bergwiesen der Rhön. Tuexenia 25:151–182

659 Phil Harvey (2016) ExifTool

660 Probst P, Wright MN, Boulesteix AL (2019) Hyperparameters and tuning strategies for  
661 random forest. Wiley Interdiscip Rev Data Min Knowl Discov 9:1–19.  
662 <https://doi.org/10.1002/widm.1301>

663 Pyšek P, Richardson DM (2011) Invasive plants. *Ecol Eng* 2011:2011–2020

664 R Core Team (2019) R: A Language and Environment for Statistical Computing

665 Royimani L, Mutanga O, Odindi J, et al (2018) Advancements in satellite remote sensing for  
666 mapping and monitoring of alien invasive plant species (AIPs). *Phys Chem Earth*.  
667 <https://doi.org/10.1016/j.pce.2018.12.004>

668 Silver M, Tiwari A, Karnieli A (2019) Identifying vegetation in arid regions using object-based  
669 image analysis with RGB-only aerial imagery. *Remote Sens* 11:1–26.  
670 <https://doi.org/10.3390/rs11192308>

671 Skowronek S, Stenzel S, Feilhauer H (2018) Detecting invasive species from above - How  
672 can we make use of remote sensing data to map invasive plant species in Germany?  
673 *Natur und Landschaft* 434–438

674 Turner D, Lucieer A, Parkes S (2017) Thermal Infrared remote sensing with a FLIR Vue Pro-  
675 R. In: *UAS4RS 2017*. Tasmania

676 Wijesingha J, Moeckel T, Hensgen F, Wachendorf M (2019) Evaluation of 3D point cloud-  
677 based models for the prediction of grassland biomass. *Int J Appl Earth Obs Geoinf*  
678 78:352–359. <https://doi.org/10.1016/J.JAG.2018.10.006>

679